

Tip-enhanced Raman scattering of glucose molecules

Zhonglin Xie[†], Chao Meng[†], Donghua Yue, Lei Xu^{*}, Ting Mei, Wending Zhang^{*}



Opto-Electronic Science

CN 51-1800/O4 ISSN 2097-0382 (Print) ISSN 2097-4000 (Online)

Tip-enhanced Raman scattering of glucose molecules

Zhonglin Xie, Chao Meng, Donghua Yue, Lei Xu, Ting Mei and Wending Zhang

Citation: Xie ZL, Meng C, Yue DH, et al. Tip-enhanced Raman scattering of glucose molecules. *Opto-Electron Sci* 4, 240027 (2025).

<https://doi.org/10.29026/oes.2025.240027>

Received: 24 October 2024; Accepted: 2 January 2025; Published online: 25 February 2025

Related articles

Ferroelectrically modulate the Fermi level of graphene oxide to enhance SERS response

Mingrui Shao, Chang Ji, Jibing Tan, Baoqiang Du, Xiaofei Zhao, Jing Yu, Baoyuan Man, Kaichen Xu, Chao Zhang, Zhen Li

Opto-Electronic Advances 2023 6, 230094 doi: [10.29026/oea.2023.230094](https://doi.org/10.29026/oea.2023.230094)

Highly sensitive and real-simultaneous CH₄/C₂H₂ dual-gas LITES sensor based on Lissajous pattern multi-pass cell

Haiyue Sun, Ying He, Shunda Qiao, Yahui Liu, Yufei Ma

Opto-Electronic Science 2024 3, 240013 doi: [10.29026/oes.2024.240013](https://doi.org/10.29026/oes.2024.240013)

Stimulated Raman scattering microscopy with phase-controlled light focusing and aberration correction for rapid and label-free, volumetric deep tissue imaging

Weiqi Wang, Zhiwei Huang

Opto-Electronic Advances 2024 7, 240064 doi: [10.29026/oea.2024.240064](https://doi.org/10.29026/oea.2024.240064)

Label-free trace detection of bio-molecules by liquid-interface assisted surface-enhanced Raman scattering using a microfluidic chip

Shi Bai, Xueli Ren, Kotaro Obata, Yoshihiro Ito, Koji Sugioka

Opto-Electronic Advances 2022 5, 210121 doi: [10.29026/oea.2022.210121](https://doi.org/10.29026/oea.2022.210121)

DOI: [10.29026/oes.2025.240027](https://doi.org/10.29026/oes.2025.240027)CSTR: [32246.14.oes.2025.240027](https://cstr.cn/32246.14.oes.2025.240027)

Tip-enhanced Raman scattering of glucose molecules

Zhonglin Xie^{1†}, Chao Meng^{1†}, Donghua Yue¹, Lei Xu^{3*}, Ting Mei¹ and Wending Zhang^{1,2*}

Glucose molecules are of great significance being one of the most important molecules in metabolic chain. However, due to the small Raman scattering cross-section and weak/non-adsorption on bare metals, accurately obtaining their "fingerprint information" remains a huge obstacle. Herein, we developed a tip-enhanced Raman scattering (TERS) technique to address this challenge. Adopting an optical fiber radial vector mode internally illuminates the plasmonic fiber tip to effectively suppress the background noise while generating a strong electric-field enhanced tip hotspot. Furthermore, the tip hotspot approaching the glucose molecules was manipulated via the shear-force feedback to provide more freedom for selecting substrates. Consequently, our TERS technique achieves the visualization of all Raman modes of glucose molecules within spectral window of 400–3200 cm^{-1} , which is not achievable through the far-field/surface-enhanced Raman, or the existing TERS techniques. Our TERS technique offers a powerful tool for accurately identifying Raman scattering of molecules, paving the way for biomolecular analysis.

Keywords: tip-enhanced Raman scattering; scanning near-field optical microscope; fiber vector light field; tip nanofocusing light source

Xie ZL, Meng C, Yue DH et al. Tip-enhanced Raman scattering of glucose molecules. *Opto-Electron Sci* 4, 240027 (2025).

Introduction

Glucose molecule is one of the most important molecules in the process of the life activities^{1–3}, and accurately obtaining its structural information is of great significance for the development of life, disease treatment, and molecular science^{4–6}. So far, many researchers have attempted to analyze the glucose molecules by the Raman scattering with the advantages of non-contact and unlabeled properties^{7,8}. Unfortunately, examining glucose molecules using Raman scattering has been proven to be extremely challenging, due to their small Raman scatter-

ing cross-section and weak adsorption/non-adsorption on bare metals⁹.

Raman scattering cross-section of glucose molecules ($5.0 \pm 1.1 - 8.9 \pm 0.9 \times 10^{-30} \text{ cm}^2 \cdot \text{molecule}^{-1} \cdot \text{sr}^{-1}$) is about five times smaller than that of the benzene molecules¹⁰, which have a large scattering cross-section of $2.8 \times 10^{-29} \text{ cm}^2 \cdot \text{molecule}^{-1} \cdot \text{sr}^{-1}$. Theoretically, the surface-enhanced Raman scattering (SERS) can amplify the Raman scattering intensity of the glucose molecules to detectable levels^{11–14}. Nevertheless, the weak/non-adsorption of glucose molecules on bare metal surfaces hinders efficient

¹Key Laboratory of Light Field Manipulation and Information Acquisition, Ministry of Industry and Information Technology, School of Physical Science and Technology, Northwestern Polytechnical University, Xi'an 710129, China; ²Research & Development Institute of Northwestern Polytechnical University in Shenzhen, Shenzhen 518063, China; ³Advanced Optics & Photonics Laboratory, Department of Engineering, School of Science & Technology, Nottingham Trent University, Nottingham NG11 8NS, United Kingdom.

[†]These authors contributed equally to this work.

Received: 24 October 2024; Accepted: 2 January 2025; Published online: 25 February 2025

interaction between the glucose molecules and the localized electric field on the metal surface. Although surface modification or functionalization methods have been proposed to facilitate the adsorption of glucose molecules on bare metal surfaces^{15–17}, the static plasmonic nanocavity characteristics of SERS lead to the random detection of only partial Raman modes of glucose molecules, accompanied by interference from Raman scattering of the bridging molecules.

Tip-enhanced Raman scattering (TERS) overcomes the limitations of the static plasmonic nanocavity in SERS^{18–21}, but current TERS techniques still appear inadequate for the glucose molecule examination. Scanning tunneling microscopy (STM)-based TERS requires the tunneling junctions between the plasmonic tip and a conductive substrate. However, the clustering characteristics of the glucose molecules hinder the formation of these tunneling junctions²². Atomic force microscope (AFM)-based TERS techniques can overcome the obstacles of the glucose molecular clusters^{23–25}, but the electric-field enhancement of the AFM-TERS is limited under the axial/side illumination and accompanied by strong background noise. This makes it difficult for the AFM-TERS to detect the weak Raman signal of the glucose molecules.

Herein, we developed a TERS platform that integrates both a feedback mechanism and a novel illumination method. The shear-force feedback of the scanning near-field microscopy (SNOM) adopted to control the tip-substrate distance does not depend on the flatness and conductivity of the substrate, offering greater flexibility in substrate selection for our SNOM-TERS. Furthermore, using the fiber-based radial vector mode (RVM) internally illuminating the plasmonic fiber tip (PFT) significantly enhances the energy conversion and suppresses the background noise. This innovation enables the creation of a background-free tip nanofocusing hotspot with the electric-field intensity amplified by two orders of magnitude. Approaching the tip hotspot to the glucose molecules located on the hydrophilic silicon, all Raman vibrational modes of the glucose molecules have been successfully visualized within the Raman window of 400–3200 cm^{-1} , consistent with the density functional theory (DFT) calculations.

Results and discussion

The home-built SNOM-TERS platform adopted an architecture of the fiber RVM internal excitation and the

lateral spectral collection is shown in Fig. 1(a1). A He-Ne laser at $\lambda=632.8$ nm was used as the excitation source. The incident direction, line width, intensity, and linearly polarized direction of the excitation light source was managed through a series of components of M, LL, A, HWP, and then coupled into a four-mode fiber (FMF) via a fiber adapter (FA). The high-order vector modes in FMF were filtered via a mode stripper (MS)²⁶, leaving only the fundamental vector mode (HE_{11}^x) in the fiber core. The HE_{11}^x mode was high efficiently converted to the RVM ($\text{TM}_{01}^{\text{OM}}$), as shown in Fig. 1(a2), via an acoustically-induced fiber grating (AIFG)²⁷, which was produced using an acoustic transducer (AT) driven by a radio frequency source (RFS). As shown in Fig. 1(b), the fiber RVM was used to internally illuminate the PFT to achieve the generation of the background-free tip hotspot^{28,29}, which was bonded on the tuning fork to approach the target analytes dispersed on the substrate (Supplementary Section 1). The tip-substrate distance was adjusted using the shear-force feedback of SNOM to enhance the Raman scattering intensity of the tip hotspot-molecules interaction process. Figure 1(c) is the scanning electric microscopy (SEM) image of a typical PFT with the tip curvature radius of 20 nm, and the background-free tip hotspot formatted at the tip apex of the PFT was photographed in Fig. 1(d).

As shown in Fig. 1(a1), the SNOM-TERS spectrum was laterally collected via a long work distance micro-objective (MO, 50 \times , $NA=0.42$, Working distance: 4 mm) and then coupled into the spectrometer via a FA after filtering the Rayleigh line by an edge filter (EF). The included angle between the PFT and the MO was determined based on the far-field scattering calculation of the tip hotspot (Supplementary Section 2). A charge coupled device (CCD) assisted by a beam splitter (BS) was adopted to monitor the position relationship between the collection light path and the PFT.

The electric-field intensity enhancement factor of the tip hotspot was calculated using the finite-time domain differenced (FDTD) method³⁰. As sketched shown in Fig. 2(a), the RVM of FMF was obtained by a boundary mode source at $\lambda=632.8$ nm and then was adopted as the internal illumination light source. The PFT has a curvature radius of 20 nm, a conic angle of 15 $^\circ$, and an Ag film thickness of 20 nm. The dielectric constant of Ag material was obtained from ref.³¹, and the refractive index of the FMF and the silicon substrate were taken from the Palik handbook³². To ensure the calculation resolution,

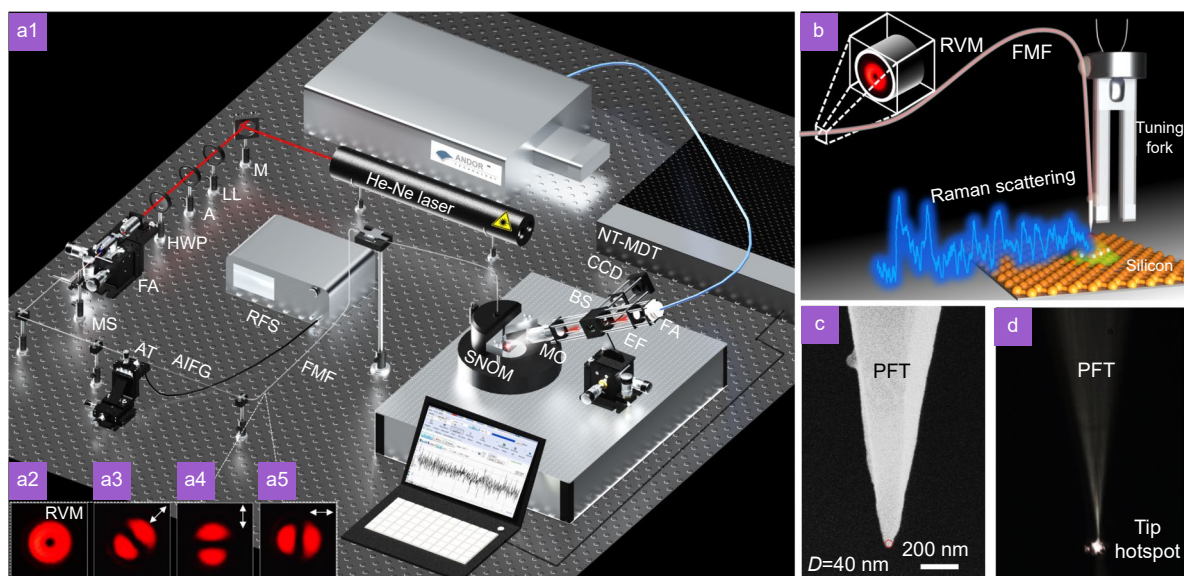


Fig. 1 | Principle of SNOM-TERS. (a1) Sketch map of SNOM-TERS platform. M: mirror, LL: laser line, A: attenuator, HWP: half-wave plate. Inset shows the transverse mode intensity of fiber RVM (a2) and the corresponding transverse electric vector distribution examinations (a3–a5). (b) PFT bundled on the tuning fork to approach silicon substrate. (c) SEM image of PFT with a tip curvature radius of 20 nm. (d) Photograph of PFT achieving background-free tip hotspot with the fiber RVM internal illumination.

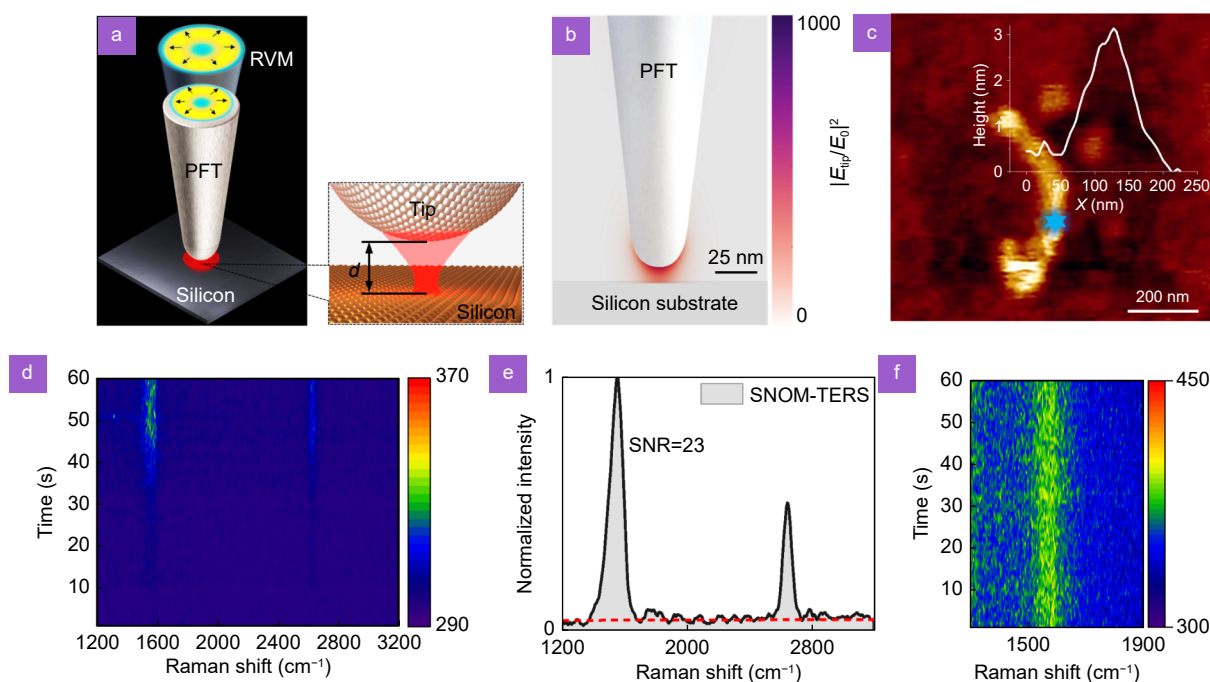


Fig. 2 | Performance evaluation of SNOM-TERS platform. (a) Illustrations of the background-free tip hotspot approaching silicon substrate with tip-substrate distance of d . (b) Calculated electric-field intensity enhancement factor $|E_{\text{tip}}/E_0|^2$ of tip hotspot in the case of $d=10$ nm and $\lambda=632.8$ nm, with E_{tip} and E_0 being of electric field of tip hotspot and fiber RVM, respectively. (c) Shear-force topography of SWCNT dispersed on a silicon substrate and (d) the corresponding time-series of SNOM-TERS spectra of SWCNT with excitation power increasing from 0 mW to 0.12 mW. Star symbol indicated the position of tip hotspot, and integration time of spectrometer was 1 s. (e) Normalized SNOM-TERS spectrum of SWCNT obtained from (d) at $t=55$ s. (f) Time-series of SNOM-TERS spectra of SWCNT with excitation power of 0.2 mW.

the tip apex region of PFT was meshed to be 0.1 nm, while gradually increased mesh scale of other areas and the transition metal boundary conditions were used to reduce the computation time.

The shear-force feedback makes it difficult to accurately obtain the variation of the tip-substrate distance, which was selected based on the data provided in the SNOM usage instructions³³. Although the nanocavity-

plasmonic mode is not formed in the nanogap, but the electric-field enhancement of the tip hotspot remains highly sensitive to the variations of the tip-substrate distance (Supplementary Section 2). **Figure 2(b)** is the calculated electric-field intensity enhancement factor $|E_{\text{tip}}/E_0|^2$ of the tip hotspot in the case of $d=10$ nm, revealing that the electric-field intensity of the tip hotspot undergoes drastic changes from the tip apex to the dielectric substrate. Additionally, it still has two orders of magnitude enhancement on the dielectric substrate surface, and the effective suppression of the background noise is sufficient to compensate for the shortcomings of the electric field intensity enhancement.

When the PFT was attached to the tuning fork, the mass and rigidity distribution of the "tuning fork+PFT" underwent significant changes, resulting in a decrease in the Q-factor of the low- and high-frequency resonance modes of the tuning fork, and the Q-factor of the high-frequency resonance mode was greater than that of the low-frequency resonance mode (Supplementary Section 3). Therefore, the high frequency resonance mode was adopted to perform the shear-force topography to better resist external environmental interference. More importantly, the transverse displacement of the "tuning fork+PFT" working in the high-frequency resonance mode was one order of magnitude smaller than that of the low-frequency resonance mode (Supplementary Section 3), ensuring that the background-free tip hotspot drove as few molecules as possible to undergo Raman scattering process. Background noise suppression of the tip hotspot was examined using the single-wall carbon nanotubes (SWCNT, Diameter: 1.2–1.7 nm) dispersed on the silicon substrate (Supplementary Section 4). **Figure 2(c)** is the shear-force topography of the SWCNT dispersed on the silicon substrate with the performance of the "tuning fork+PFT" being of previously validated by the standard samples (Supplementary Section 5). By increasing the excitation power from 0 mW to 0.12 mW, a time series of the SNOM-TERS spectra was obtained, as shown in **Fig. 2(d)**. The signal-noise ratio (SNR) of the extracted spectra (**Fig. 2(e)**) was quantitatively analyzed to be $\text{SNR}=23$ (1556 cm^{-1}), which was three times higher than that of the far-field Raman spectrum of the SWCNT (Supplementary Section 4). With the excitation power being of maintained at 0.2 mW, the time-series of SNOM-TERS spectra of the SWCNT at 1556 cm^{-1} was examined, as shown in **Fig. 2(f)**. The relative standard deviation of the Raman signal intensity was estimated to

be 4.7%, exhibiting that the SNOM-TERS platform retained excellent time stability.

Based on the home-built SNOM-TERS platform, the "fingerprint information" of the glucose molecules was examined. To eliminate the interference of the bridging molecules, the noble metallic substrate was replaced by the hydrophilic silicon (Method 2) with the hydroxyl group effectively adsorbing the glucose molecules. **Figure 3(a)** is the shear-force topography of the glucose molecules on the hydrophilic silicon (Method 3), revealing that the hydroxyl groups of the glucose molecules result in clusters on the hydrophilic silicon, rather than monolayers. **Figure 3(b)** is a typical three-dimensional morphology distribution of one glucose molecule cluster with a height of ~ 25 nm (**Fig. 3(c)**). Furthermore, the far-field Raman scattering spectra of the glucose molecules dispersed on the silicon and the hydrophilic silicon, as shown in **Fig. 3(d)**, furtherly proving that the effectively adsorption of the glucose molecules on the hydrophilic silicon. With the background-free tip hotspot approaching the top of the glucose molecules cluster, the time-series of the SNOM-TERS spectra was obtained within the spectral window of $400\text{--}2000\text{ cm}^{-1}$, as shown in **Fig. 3(e)**, with the excitation power increasing from 0.1 mW to 0.25 mW. The visualized Raman modes gradually increased as the intensity of the tip hotspot gradually increased. With the excitation power being of maintained at 0.25 mW, a SNOM-TERS spectrum of the glucose molecules within the spectral window of $400\text{--}3200\text{ cm}^{-1}$ was examined, as shown in **Fig. 3(f)**, and the inset shows a partial enlargement of the spectral recording window ($400\text{--}2000\text{ cm}^{-1}$) with weak Raman scattering intensity. Note that, the stretching vibration of C=O functional group ($\sim 1750\text{ cm}^{-1}$) of the chain glucose molecules has been clearly observed, consistent with the DFT calculations (**Fig. 3(g)**). The D-(+)-glucose molecules can be formed by the chain glucose molecules that undergo internal reactions, where the interaction between C=O and -OH groups cause C=O change to C-O, leading to the inability to observe Raman peak of C=O functional group ($\sim 1750\text{ cm}^{-1}$).

Because of the low resolution of the spectrometer during the broadband spectrum operation, the SNOM-TERS spectrum of the chain glucose molecules exhibited a wide peak with multiple sharp peaks (**Fig. 3(f)**). To clearly distinguish the multiple Raman vibrational modes, multiple peaks Gaussian fitting on the SNOM-TERS spectrum was performed within twelve segmental Raman

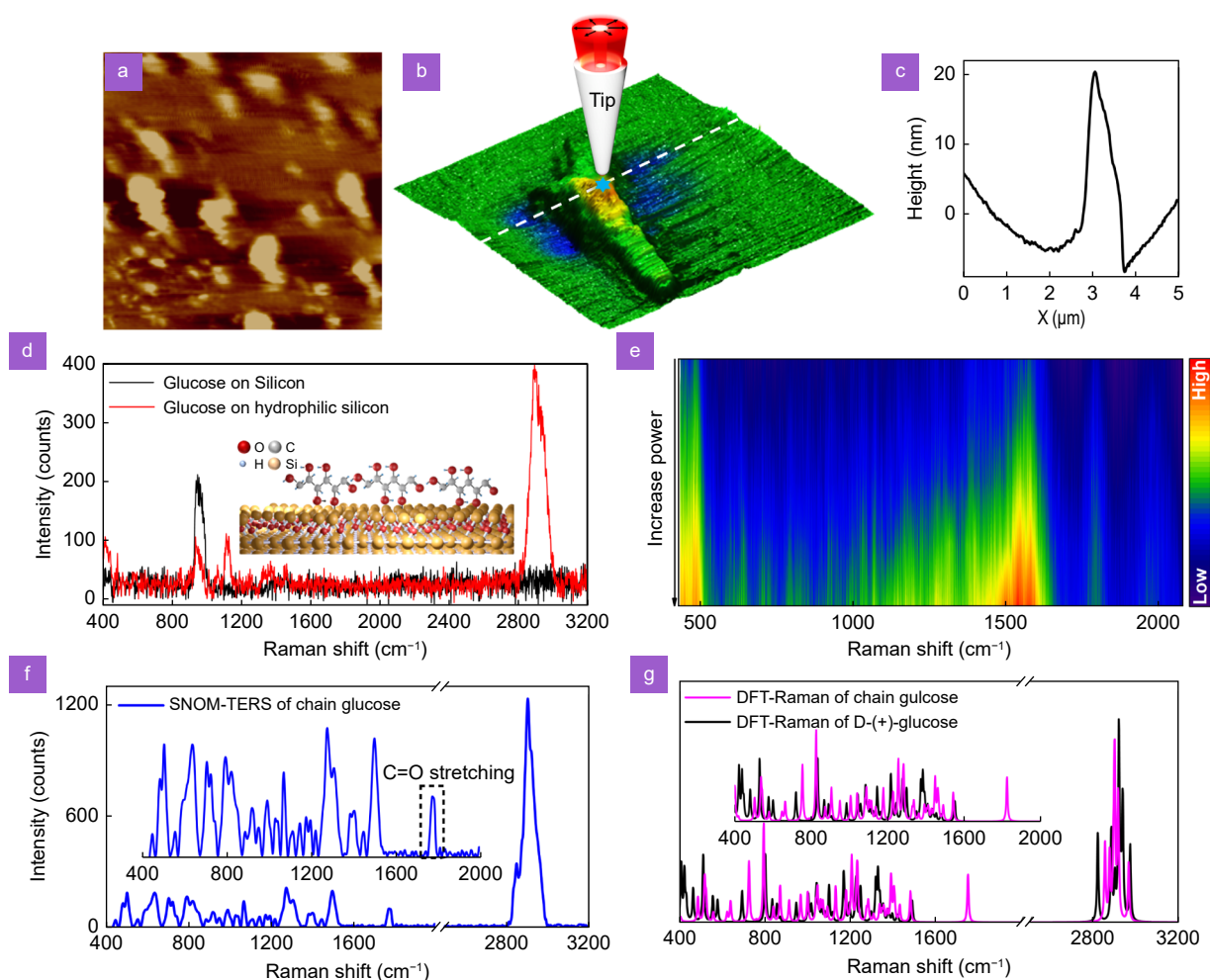


Fig. 3 | Fingerprint information acquisition of glucose molecules. (a) Shear-force topography ($15\ \mu\text{m}\times 15\ \mu\text{m}$) of glucose molecules clustered on a hydrophilic silicon substrate and (b) a typical three-dimensional morphology distribution ($5\ \mu\text{m}\times 5\ \mu\text{m}$). (c) Height distribution of glucose molecule cluster obtained along a dashed white line in (b). (d) Far-field Raman spectra of glucose molecules clustered on silicon (black curve) and hydrophilic silicon (red curve) substrates. Inset is an illustration of glucose molecules adsorbed efficiently on hydrophilic silicon, and the integration time of spectrometer was 20 s. (e) Time-series of SNOM-TERS spectra of glucose molecular cluster with excitation power increasing from 0.1 mW to 0.25 mW, and the integration time of spectrometer was 120 s. (f) SNOM-TERS spectrum with PFT approaching glucose molecules cluster and locating at the position indicated by star symbol in (b). Excitation power was 0.25 mW, and integration time of spectrometer was 120 s. (g) DFT-calculated Raman spectra of chain and D-(+)-glucose molecules (Method 1) with chemical structures of two types of glucose molecules being shown in Fig. S10.

windows and compared detailedly with the DFT-Raman calculation results for each segmental Raman window, as shown in Fig. 4. The comparison between the DFT-calculation and the SNOM-TERS Raman vibrational modes of the chain glucose molecules was summarized in Supplementary Table S1. All Raman vibrational modes (thirty-four) of the chain glucose molecules have been effectively visualized within a spectral recording window by our developed SNOM-TERS platform, while this visualization was not achievable with the conventional far-field excitation Raman, SERS, and STM-TERS (Supplementary Section 6). Unlike previous studies that randomly

observed the vibrational modes of glucose molecules^{34,35}, our SNOM-TERS approach allows for the simultaneous visualization of Raman vibrational modes in glucose molecules. Compared with SERS technology, the SNOM-TERS can avoid the interference of bridging molecules in Raman spectrum, and by adjusting the spatial relationship between the background-free tip hotspot and the glucose molecules (Supplementary Section 7), the excitation efficiency and SNR of Raman spectra of the glucose molecule can be significantly improved. In addition, compared with STM-TERS technology, the shear-force feedback mechanism of SNOM-TERS can position the

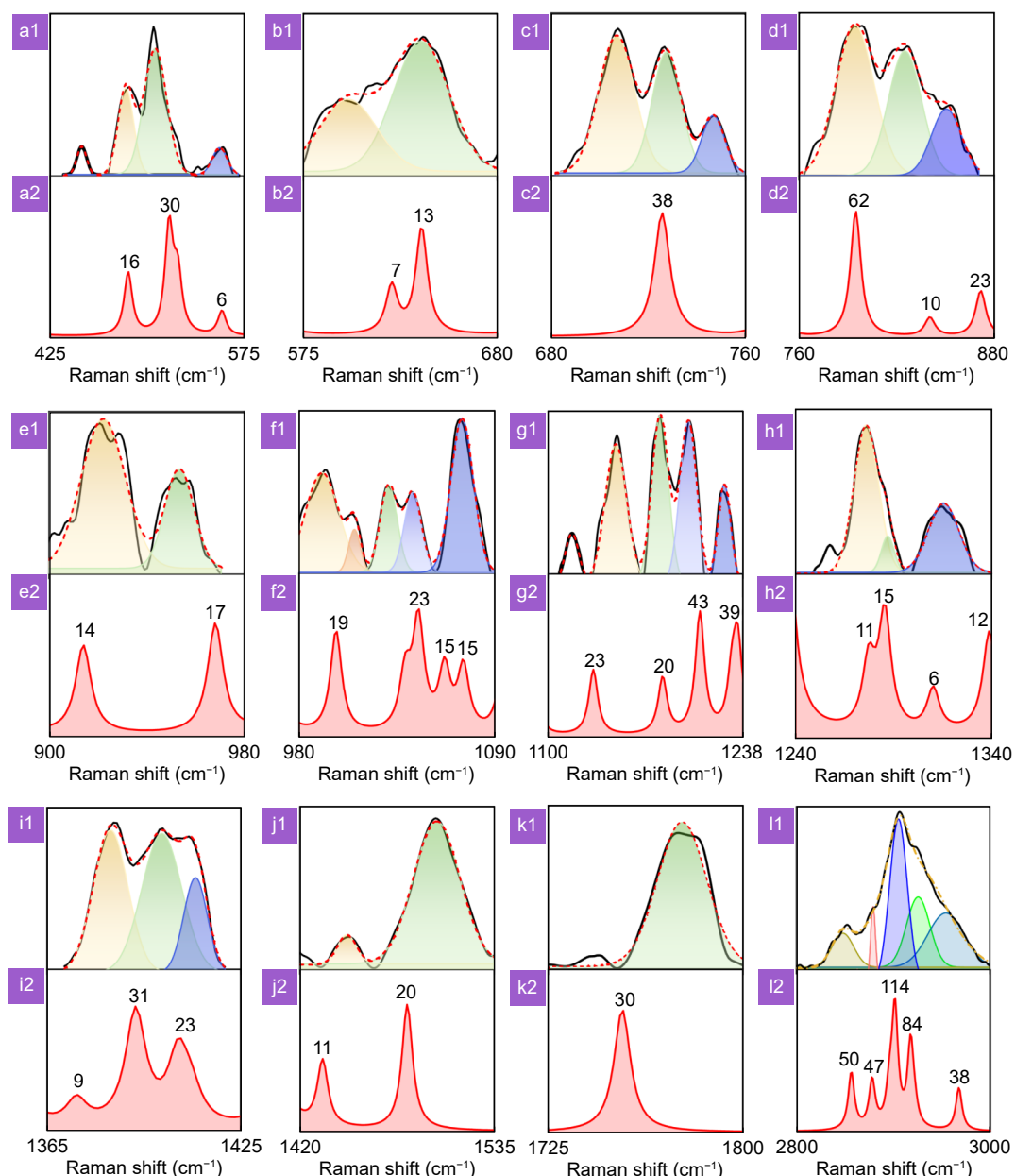


Fig. 4 | Vibrational modes identification of chain glucose molecules. Multi-peak Gaussian curve-fitting analysis of SNOM-TERS spectrum of chain glucose molecules within (a1–l1) twelve spectral windows and (a2–l2) corresponding DFT calculations.

background-free tip hotspot on the surface of the glucose molecules cluster, thereby achieving efficient excitation of TERS spectrum of glucose molecules.

Due to the small Raman scattering cross-section of the glucose molecules, a longer integration time was required to obtain the effective SNOM-TERS signals, which placed higher demands on the time stability of the SNOM-TERS platform. The Raman window (2800–3000 cm^{-1}) with strong Raman activity was selected to assess the time stability of the SNOM-TERS platform. As shown in Fig. 4(l1), the decomposed Gaussian fitting re-

sults of the SNOM-TERS spectrum involve five vibrational modes, coinciding with the DFT calculations (Fig. 4(l2)). The highly active Raman mode ($\sim 2906 \text{ cm}^{-1}$) associated with C1,2,3,4,5-H stretching vibration was selected to time mapping. The relative standard deviation of the Raman scattering intensity was calculated to be 2.8% (Supplementary Section 8), indicating the excellent time stability of the SNOM-TERS platform.

Conclusion

In summary, the vibrational modes of glucose molecules

have been effectively visualized using our developed SNOM-TERS platform. The shear-force feedback overcomes the clustering characteristics of the glucose molecules and drives the PFT to approach the surface of the molecular cluster. The background-free tip hotspot with significant electric-field intensity enhancement effectively solves the small Raman scattering cross-section of the glucose molecules and increases the SNR of Raman scattering, resulting in all vibrational modes of the glucose molecules being simultaneously visualized within the Raman recording window. The examination of vibrational modes of the glucose molecules is of great significance for the development of life, disease treatment, and molecular science. Our SNOM-TERS technology provides an effective and promising platform for accurately identifying the near-field Raman scattering of molecules and expands the applicability of TERS technique.

Experimental methods

Calculations of vibrational modes of glucose molecule

The model of a glucose molecule was constructed using the Chem 3D software, and the Raman spectrum of a glucose molecule in the gas phase was calculated using the DFT³⁶, B3LYP functional, and the 6-31G (d) group set in Gaussian 09 software. The vibrational modes corresponding to each Raman peak of the glucose molecules were obtained from the Result-Vibrations function window of Gaussian View software and scaled by a frequency scaling factor of 0.9613. The Gaussian output file was imported into the Multiwfn software to calculate the Raman intensity of each vibrational mode at 300 K and 632.8 nm excitation³⁷.

Hydrophilic silicon

Hydrophilic treatment of silicon originated from ref.³⁸. A silicon wafer was soaked in a 100 °C piranha solution (concentrated H₂SO₄:30% H₂O₂ volume ratio=7:3) for 30 minutes for hydrophilic treatment, and then the silicon wafer was placed in the ultrapure water for ultrasound of 5 minutes to remove the surface residues. [Figure S15](#) shows the Raman spectra of the silicon (black curve) and the hydrophilic-treated silicon (red curve), revealing that the hydrophilic silicon does not introduce additional Raman vibrational modes.

Samples preparation

Glucose powder was purchased from Aladdin. 180 mg of the glucose powder was added to 10 mL of the ultrapure water to obtain the glucose solution (10⁻¹ mol/L). The hydrophilic treated silicon was soaked in the glucose solution for 24 hours, and then the remaining moisture on the silicon wafer was blown dry with nitrogen gas. [Figure 3\(d\)](#) is the Raman spectrum of the glucose molecules deposited on the silicon (black curve) and the hydrophilic silicon (red curve). Compared with the silicon substrate, more vibrational modes of glucose molecules can be examined on the hydrophilic silicon substrate, which indirectly indicates the effective adsorption of the glucose molecules on the hydrophilic silicon.

References

1. Levy T, Voeltzke K, Hruby L et al. mTORC1 regulates cell survival under glucose starvation through 4EBP1/2-mediated translational reprogramming of fatty acid metabolism. *Nat Commun* **15**, 4083 (2024).
2. Prahalad P, Scheinker D, Desai M et al. Equitable implementation of a precision digital health program for glucose management in individuals with newly diagnosed type 1 diabetes. *Nat Med* **30**, 2067–2075 (2024).
3. Zou K, Rouskin S, Dervishi K et al. Life span extension by glucose restriction is abrogated by methionine supplementation: cross-talk between glucose and methionine and implication of methionine as a key regulator of life span. *Sci Adv* **6**, eaba1306 (2020).
4. Ibrahim MA, Allam M, El-Haes H et al. Analysis of the structure and vibrational spectra of glucose and fructose. *Eclat Quim* **31**, 15–21 (2006).
5. Lewis BE, Schramm VL. Conformational equilibrium isotope effects in glucose by ¹³C NMR spectroscopy and computational studies. *J Am Chem Soc* **123**, 1327–1336 (2001).
6. Zhang T, Li YT, Lv XM et al. Ultra-sensitive and unlabeled SERS nanosheets for specific identification of glucose in body fluids. *Adv Funct Mater* **34**, 2315668 (2024).
7. Yang D, Afroosheh S, Lee JO et al. Glucose sensing using surface-enhanced Raman-mode constraining. *Anal Chem* **90**, 14269–14278 (2018).
8. Ahmadianyazdi A, Lan Nguyen NH, Xu J et al. Glucose measurement via Raman spectroscopy of graphene: principles and operation. *Nano Res* **15**, 8697–8704 (2022).
9. Sun XC. Glucose detection through surface-enhanced Raman spectroscopy: a review. *Anal Chim Acta* **1206**, 339226 (2022).
10. Shafer-Peltier KE, Haynes CL, Glucksberg MR et al. Toward a glucose biosensor based on surface-enhanced Raman scattering. *J Am Chem Soc* **125**, 588–593 (2003).
11. Sooraj KP, Ranjan M, Rao R et al. SERS based detection of glucose with lower concentration than blood glucose level using plasmonic nanoparticle arrays. *Appl Surf Sci* **447**, 576–581 (2018).
12. Shao MR, Ji C, Tan JB et al. Ferroelectrically modulate the Fermi level of graphene oxide to enhance SERS response. *Opto-Electron Adv* **6**, 230094 (2023).

13. Wang WQ, Huang ZW. Stimulated Raman scattering microscopy with phase-controlled light focusing and aberration correction for rapid and label-free, volumetric deep tissue imaging. *Opto-Electronic Adv* 7, 240064 (2024).
14. Li SS, Fang YN, Wang JF. Control of light-matter interactions in two-dimensional materials with nanoparticle-on-mirror structures. *Opto-Electron Sci* 3, 240011 (2024).
15. Stuart DA, Yuen JM, Shah N et al. In vivo glucose measurement by surface-enhanced Raman spectroscopy. *Anal Chem* 78, 7211–7215 (2006).
16. Rycenga M, McLellan JM, Xia YN. A SERS study of the molecular structure of alkanethiol monolayers on Ag nanocubes in the presence of aqueous glucose. *Chem Phys Lett* 463, 166–171 (2008).
17. Ham J, Yun BJ, Koh WG. SERS-based biosensing platform using shape-coded hydrogel microparticles incorporating silver nanoparticles. *Sens Actuators B Chem* 341, 129989 (2021).
18. Meng QS, Zhang JX, Zhang Y et al. Local heating and Raman thermometry in a single molecule. *Sci Adv* 10, ead1015 (2024).
19. Imada H, Imai-Imada M, Miwa K et al. Single-molecule laser nanospectroscopy with micro-electron volt energy resolution. *Science* 373, 95–98 (2021).
20. Zhang R, Zhang Y, Dong ZC et al. Chemical mapping of a single molecule by plasmon-enhanced Raman scattering. *Nature* 498, 82–86 (2013).
21. Lee J, Crampton KT, Tallarida N et al. Visualizing vibrational normal modes of a single molecule with atomically confined light. *Nature* 568, 78–82 (2019).
22. Chen C, Li WZ, Song YC et al. Formation of water and glucose clusters by hydrogen bonds in glucose aqueous solutions. *Comput Theor Chem* 984, 85–92 (2012).
23. Deckert-Gaudig T, Kämmer E, Deckert V. Tracking of nanoscale structural variations on a single amyloid fibril with tip-enhanced Raman scattering. *J Biophotonics* 5, 215–219 (2012).
24. Ma XZ, Zhu YZ, Yu N et al. Toward high-contrast atomic force microscopy-tip-enhanced Raman spectroscopy imaging: nanoantenna-mediated remote-excitation on sharp-tip silver nanowire probes. *Nano Lett* 19, 100–107 (2019).
25. Berweger S, Atkin JM, Olmon RL et al. Adiabatic tip-plasmon focusing for nano-Raman spectroscopy. *J Phys Chem Lett* 1, 3427–3432 (2010).
26. Zhang WD, Huang LG, Wei KY et al. High-order optical vortex generation in a few-mode fiber via cascaded acoustically driven vector mode conversion. *Opt Lett* 41, 5082–5085 (2016).
27. Zhang WD, Huang LG, Wei KY et al. Cylindrical vector beam generation in fiber with mode selectivity and wavelength tunability over broadband by acoustic flexural wave. *Opt Express* 24, 10376–10384 (2016).
28. Liu M, Lu FF, Zhang WD et al. Highly efficient plasmonic nanofocusing on a metallized fiber tip with internal illumination of the radial vector mode using an acousto-optic coupling approach. *Nanophotonics* 8, 921–929 (2019).
29. Lu FF, Zhang WD, Huang LG et al. Mode evolution and nanofocusing of grating-coupled surface plasmon polaritons on metallic tip. *Opto-Electron Adv* 1, 180010 (2018).
30. Oskooi AF, Roundy D, Ibanescu M et al. MEEP: a flexible free-software package for electromagnetic simulations by the FDTD method. *Comput Phys Commun* 181, 687–702 (2010).
31. Haynes WM. *CRC Handbook of Chemistry and Physics* (CRC Press, Boca Raton, 2016).
32. Palik ED. *Handbook of Optical Constants of Solids* (Academic Press, Orlando, 1985).
33. Karrai K, Grober RD. Piezoelectric tip-sample distance control for near field optical microscopes. *Appl Phys Lett* 66, 1842–1844 (1995).
34. Wang X, Zhang AH, Zhi MC et al. Glucose concentration measured by the hybrid coherent anti-Stokes Raman-scattering technique. *Phys Rev A* 81, 013813 (2010).
35. Kang JW, Park YS, Chang H et al. Direct observation of glucose fingerprint using in vivo Raman spectroscopy. *Sci Adv* 6, eaay5206 (2020).
36. Hariharan PC, Pople JA. Accuracy of AH_n equilibrium geometries by single determinant molecular orbital theory. *Mol Phys* 27, 209–214 (1974).
37. Lu T, Chen FW. Multiwfn: a multifunctional wavefunction analyzer. *J Comput Chem* 33, 580–592 (2012).
38. Kobayashi K, Unno H, Takizawa H et al. Chemical treatment effect of Si (111) surfaces in H_2SO_4 : H_2O_2 solution. *Jpn J Appl Phys* 35, 5925–5928 (1996).

Acknowledgements

This work was supported by National Natural Science Foundation of China (12374358, 91950207), Guangdong Basic and Applied Basic Research Foundation (2024A1515010420).

Author contributions

Z.L.X. and C.M. built the experimental configuration, performed the experiments. L.X. and T.M. analyzed the data. Z.L.X. performed electromagnetic field calculations. C.M. performed DFT calculations. D.H.Y. performed Investigation. W.D.Z. designed and supervised the work. All authors discussed the results and contributed to the writing of the manuscript.

Competing interests

The authors declare no competing financial interests.